ChemPubSoc Europe

DOI: 10.1002/ejic.201700054

EurJIC European Journal of Inorganic Chemistry

Full Paper

Xenon Fluorides

Photochemical Synthesis and Characterization of Xenon(VI) Hexafluoridomanganates(IV)

Zoran Mazej,*[a] Evgeny Goreshnik,[a] Zvonko Jagličić,[b] Yaroslav Filinchuk,[c] Nikolay Tumanov,[c,d] and Lev G. Akselrud[e]

Abstract: Reactions between XeF_2, MnF_3 and UV-irradiated elemental F_2 in anhydrous HF have yielded $[XeF_5]_2[MnF_6]$ and XeF_5MnF_5; meanwhile, $[XeF_5]_4[Mn_8F_{36}]$ has been observed as a minor phase upon the crystallization of the product obtained by fluorination of an $n(XeF_2)/n(MnF_3)$ = 1:3 mixture in the presence of an UV source. The crystal structure of $[XeF_5]_2[MnF_6]$ is isotypic with the known $[XeF_5]_2[PdF_6]$. Its asymmetric structural unit consists of two crystallographically unique $[XeF_5]^+$ cations and a $[MnF_6]^{2-}$ anion. The single-crystal structure determination of $XeF_6{\cdot}2MnF_4$ reveals that it is better formulated as $[XeF_5]_4[Mn_8F_{36}]$. Discrete octameric $[Mn_8F_{36}]^{4-}$ anions are built from eight MnF_6 octahedra, each sharing three vertices, in the shape of a ring, which is different from the previously known cubic $[Ti_8F_{36}]^{4-}$ anion. The main structural feature of the anionic part of the crystal structure of $[XeF_5][MnF_5]$ (determined from both X-ray single-crystal and synchrotron X-ray powder diffraction data) is infinite zigzag chains of distorted MnF_6 octahedra that share *cis* vertices. $[XeF_5][MnF_5]$ is paramagnetic in the 296–200 K temperature range, with a Curie constant of C = 1.87 emu K mol^{-1} (μ_{eff} = 3.87 μ_B) and a Curie–Weiss temperature of θ = –9.3 K. Below 100 K, there is weak antiferromagnetic coupling between the Mn^{IV} ions, with a coupling constant of J = –1.3 cm^{-1}. Raman spectra showed that $[XeF_5]_2[MnF_6]$ decomposes at ambient temperature in a He–Ne laser beam (power > 1.7 mW) to $[XeF_5][MnF_5]$, with further decomposition to MnF_3.

Introduction

In 1970, Aubert and Cady reported high-temperature fluorinations of a Mn and Xe mixture by elemental fluorine at high pressure.[1] They found that a complex was formed; however, they were not sure about the oxidation state of manganese (III or IV). Six years later, Bohinc et al.[2] reported a much more extensive study on the reactions between MnF_2 and excessive XeF_6 at 60 °C. The obtained compounds, formulated as $4XeF_6{\cdot}MnF_4$, $2XeF_6{\cdot}MnF_4$, $XeF_6{\cdot}MnF_4$ and $XeF_6{\cdot}2MnF_4$, were characterized by total chemical elemental analysis, IR spectroscopy and magnetic susceptibility measurements. Although characterization with X-ray powder diffraction patterns was also mentioned, no data are available.[2] Much later, thermal decomposition of $4XeF_6{\cdot}MnF_4$ was studied.[3]

In the XeF_6/TiF_4 system, it has been already shown how previously formulated $XeF_6{\cdot}TiF_4$ and $XeF_6{\cdot}2TiF_4$[4] are more correctly described as $[XeF_5][TiF_5]$ and $[XeF_5]_5[Ti_{10}F_{45}]$, respectively.[5] Similarly, $3XeF_6{\cdot}4TiF_4$ and $XeF_6{\cdot}3TiF_4$ correspond to $[XeF_5]_3[Ti_4F_{19}]$ and $[XeF_5][Ti_3F_{13}]$, respectively.[5,6] The anionic parts in the crystal structures of $[XeF_5][TiF_5]$ and $[XeF_5][Ti_3F_{13}]$ are polymeric; that is, there are $([TiF_5]^-)_\infty$ infinite chains for the former and $([Ti_3F_{13}]^-)_\infty$ infinite columns for the latter. The crystal structures of $[XeF_5]_3[Ti_4F_{19}]$ and $[XeF_5]_5[Ti_{10}F_{45}]$ consist of $[XeF_5]^+$ cations and discrete $[Ti_4F_{19}]^{3-}$ and $[Ti_{10}F_{45}]^{5-}$ anions. The $[Ti_{10}F_{45}]^{5-}$ anion is the largest known example of a discrete oligomeric perfluorometallate anion with the highest rate of association of $[M^{n+}F_6]^{n-6}$ octahedra.

On the basis of vibrational spectroscopic data, it has been concluded that $4XeF_6{\cdot}MnF_4$ is $[Xe_2F_{11}]_2[MnF_6]$ and the 2:1 compound ($2XeF_6{\cdot}MnF_4$) corresponds to $[XeF_5]_2[MnF_6]$.[3] Since no structural data have been available for the $4XeF_6{\cdot}MnF_4$, $2XeF_6{\cdot}MnF_4$, $XeF_6{\cdot}MnF_4$ and $XeF_6{\cdot}2MnF_4$ phases, we were interested to find what is, in reality, hidden behind these simple formulas and whether the determined structures of Mn compounds would be isostructural with titanium ones[5,6] or whether a new structure type would be obtained by the larger Mn^{4+}. The results are described in this paper.

[a] *Department of Inorganic Chemistry and Technology, Jožef Stefan Institute, Jamova 39, 1000 Ljubljana, Slovenia*
E-mail: zoran.mazej@ijs.si
http://k1.ijs.si/en/
https://www.ijs.si/ijsw/V001/JSI
[b] *Faculty of Civil and Geodetic Engineering, University of Ljubljana, Institute of Mathematics, Physics and Mechanics, Jadranska 19, 1000 Ljubljana, Slovenia*
[c] *Institute of Condensed Matter and Nanosciences, Université catholique de Louvain, Place L. Pasteur 1, 1348 Louvain-la-Neuve, Belgium*
[d] *Department of Chemistry, University of Namur, Rue de Bruxelles 61, 5000 Namur, Belgium*
[e] *Department of Inorganic Chemistry, Ivan Franko National University of Lviv, Kyryla and Mefodia Str. 6, 79005 Lviv, Ukraine*
Supporting information and ORCID(s) from the author(s) for this article are available on the WWW under https://doi.org/10.1002/ejic.201700054.

Results and Discussion

Photochemical Synthesis and Crystal Growth of Xenon(VI) Hexafluoridomanganates(IV)

Various amounts of xenon(II) fluoride and manganese(III) fluoride mixtures were fluorinated by the use of UV-irradiated elemental fluorine (Table 1 and Table S1 in the Supporting Information). The light-absorption maximum of the F_2 molecule is close to 300 nm, with a broad tail into the visible region. This absorption is associated with promotion of the electron from a bonding to a nonbonding molecular orbital. The consequence is the dissociation of the F_2 molecule to $F^{\cdot}$ radicals, which can react with substances in anhydrous HF (aHF), resulting in compounds in the highest oxidation states [Equation (1)].[7]

$$XeF_2 + MnF_3 + nF_2 \xrightarrow[298\ K]{\text{aHF, UV}} nXeF_6{\cdot}MnF_4 \quad (1)$$

Table 1. Xenon(VI) hexafluoridomanganates(IV) detected in the isolated solids after reactions or crystallizations of various $nXeF_2/MnF_3$/UV-irradiated F_2/aHF mixtures.

$n(XeF_2)/n(MnF_3)$ molar ratio	Colour of aHF solution	Observed crystalline phases[a]
4:1	light orange	$[XeF_5]_2[MnF_6]$
2:1	orange	$[XeF_5]_2[MnF_6]$
1:1	red–orange	$[XeF_5][MnF_5]$
1:2	red[b]	$[XeF_5][MnF_5]$[c]
1:3	red[b]	$[XeF_5][MnF_5]$, $[XeF_5]_4[Mn_8F_{36}]$[c,d]
1:4	red[b]	$[XeF_5][MnF_5]$[c]

[a] Unit cells of grown crystals were checked with an X-ray diffractometer. There is always a possibility that phases present in minor amounts were overlooked. [b] Undissolved red material was also visible. [c] Powdered red-coloured material was also present. [d] Only a few single crystals of $[XeF_5]_4[Mn_8F_{36}]$ were observed.

Under applied experimental conditions, only $[XeF_5]_2[MnF_6]$ and $[XeF_5][MnF_5]$ can be synthesized in a pure state from the corresponding $n(XeF_2)/n(MnF_3)$ ratios (Table 1). We have not been able to isolate $[Xe_2F_{11}]_2[MnF_6]$ ($4XeF_6{\cdot}MnF_4$), which can be prepared by a reaction between MnF_2 and an excess of XeF_6 at 60 °C.[2] However, light-orange $[Xe_2F_{11}]_2[MnF_6]$ is not stable at room temperature, and it loses XeF_6, yielding orange $[XeF_5]_2[MnF_6]$.[3] When the amount of MnF_3 was increased above the 1:1 ratio (Table 1), $[XeF_5][MnF_5]$ was detected in all isolated solids. Only in one case, were a few single crystals $[XeF_5]_4[Mn_8F_{36}]$ found in the mixture of $[XeF_5][MnF_5]$ and some powdered material. The latter has not been investigated, but it most likely consists of MnF_4. In the presence of an UV source, MnF_3 is completely oxidized by photodissociated F_2 in aHF to MnF_4.[8]

In the cases of various perfluorotitanate(IV) compounds, Raman spectroscopy was found to be the most appropriate method for the identification of various perfluorotitanate(IV) phases. In the case of Mn compounds, there is a problem of their extreme sensibility to the power of the laser beam. Therefore, the spectra were measured at ambient temperature at the lowest power of the laser beam at which it was still possible to observe vibrational bands (see Figures S1 and S2 in the Supporting Information). The Raman spectra of $[XeF_5]_2[MnF_6]$ and $[XeF_5][MnF_5]$ are both of very poor quality. However, they both confirm the presence of $[XeF_5]^+$ cations. The Raman spectrum of $[XeF_5][MnF_5]$ shows a strong band at 712 cm^{-1}, which can be assigned to Mn–F vibrations. One of the strong bands in the 595–600 cm^{-1} region in the Raman spectrum of $[XeF_5]_2[MnF_6]$ most likely belongs to $[MnF_6]^{2-}$. The Raman spectrum of $[XeF_5]_2[MnF_6]$ is in agreement with the previously known Raman spectra of $[XeF_5]_2[MnF_6]$, which was prepared by a reaction between MnF_2, XeF_6 and KrF_2 in aHF and by a reaction between MnO_3F and XeF_6 in aHF (see Figures S3 and S4). With increasing power of the laser beam, $[XeF_5]_2[MnF_6]$ decomposes to $[XeF_5][MnF_5]$ and the latter decomposes to MnF_3. A similar trend was observed during the thermal decomposition of $[XeF_5]_2[MnF_6]$.[3]

Crystal Structures of $[XeF_5]_2[MnF_6]$, $[XeF_5]_4[Mn_4F_{38}]$ and $[XeF_5][MnF_5]$

The corresponding crystal data and refinement results are summarized in Tables 2 and 3.

Table 2. Crystal data and refinement results for $[XeF_5]_2[MnF_6]$ and $[XeF_5]_4[Mn_4F_{38}]$.

Chemical formula	$[XeF_5]_2[MnF_6]$	$[XeF_5]_4[Mn_4F_{38}]$	$[XeF_5]_4[Mn_4F_{38}]$
Fw [g mol^{-1}]	621.50	2028.68	2028.68
Crystal system	orthorhombic	monoclinic	monoclinic
Space group	$Pca2_1$[a]	$P2_1/c$	$P2_1/c$
a [Å]	9.2567(3)	9.34476(12)	9.4548(5)
b [Å]	12.5955(4)	17.9511(2)	18.0029(8)
c [Å]	9.2199(3)	11.93831(15)	11.9797(7)
α [°]	90	90	90
β [°]	90	99.5339(12)	100.622(5)
γ [°]	90	90	90
V [Å^3]	1074.96(6)	1974.98(4)	2004.18(18)
Z	4	2	2
$D_{calcd.}$ [g cm^{-3}]	3.8399	3.4109	3.3612
T [K]	150	150	296
R_1[b]	0.0159	0.0248	0.0476
wR_2[c]	0.0328	0.0523	0.1126

[a] Taking into account a rather high Flack parameter of 0.396(17), the structure has been refined as a racemic twin. [b] R_1 is defined as $\Sigma||F_o| - |F_c||/\Sigma|F_o|$ for $I > 2\sigma(I)$. [c] wR_2 is defined as $\{\Sigma[w(F_o^2 - F_c^2)^2]/\Sigma w(F_o^2)^2\}^{1/2}$.

Table 3. Crystal data and refinement results for XeF_5MnF_5.

Chemical formula	$[XeF_5][MnF_5]$[a]	$[XeF_5][MnF_5]$[b]	$[XeF_5][MnF_5]$[b]	$[XeF_5][MnF_5]$[b]
Fw [g mol^{-1}]	1504.92	1504.92	1504.92	1504.92
Crystal system	monoclinic	monoclinic	monoclinic	monoclinic
Space group	$P2_1/c$	$P2_1/c$	$P2_1/c$	$P2_1/c$
a [Å]	9.0056(4)	9.0265(5)	9.075(1)	9.0901(9)
b [Å]	17.8909(8)	17.8898(9)	17.952(2)	17.953(2)
c [Å]	8.3748(3)	8.3506(5)	8.368(1)	8.3728(8)
α [°]	90	90	90	90
β [°]	90.079(4)	90.132(5)	90.163(8)	90.168(8)
γ [°]	90	90	90	90
V [Å^3]	1349.34(10)	1348.4(2)	1363.5(5)	1366.4(4)
Z	2	2	2	2
$D_{calcd.}$ [g cm^{-3}]	3.704	3.7061	3.6651	3.6574
T [K]	150	120	150	200
R_1[c]	0.0942	–	–	–
wR_2[d]	0.2587	–	–	–
$R_{I(CSD)}$[e]	–	0.0557	0.0828	0.0914
R_P[f]	–	0.0436	0.0450	0.0467
R_{wP}[g]	–	0.0605	0.0643	0.0643
$R_{P(CSD)}$[h]	–	0.1084	0.1277	0.1325
$R_{wP(CSD)}$[i]	–	0.1102	0.1291	0.1408

[a] Single-crystal data. [b] Synchrotron X-ray powder diffraction. [c] R_1 is defined as $\Sigma||F_o| - |F_c||/\Sigma|F_o|$ for $I > 2\sigma(I)$. [d] wR_2 is defined as $\{\Sigma[w(F_o^2 - F_c^2)^2]/\Sigma w(F_o^2)^2\}^{1/2}$. [e] R_I for powder diffraction is defined as $[\Sigma|(I_{ko})^{1/2} - (I_{kc})^{1/2}|/\Sigma(I_{ko})^{1/2}]$. [f] R_P for powder diffraction is defined as $[\Sigma|(y_{io}) - (y_{ic})|/\Sigma(y_{io})]$. [g] R_{wP} for powder diffraction is defined as $\{\Sigma w_i[(y_{io}) - (y_{ic})]^2/\Sigma w_i(y_{io})^2\}^{1/2}$. [h] $R_{P(CSD)}$, calculated by WinCSD software,[9] includes a background component of intensity and it is defined as $[\Sigma|(y_{io}) - (y_{ic})|/\Sigma(y_{io} - y_{iF})]$. [i] $R_{wP(CSD)}$, calculated by WinCSD software,[9] includes a background component of intensity and it is defined as $\{\Sigma w_i[(y_{io}) - (y_{ic})]^2/\Sigma w_i(y_{io} - y_{iF})^2\}^{1/2}$.

Crystal Structure of $(XeF_5)_2MnF_6$

The crystal structure of $[XeF_5]_2[MnF_6]$ is isotypic with $[XeF_5]_2[PdF_6]$ {orthorhombic, $Pca2_1$, $Z = 4$, $a = 9.346(6)$ Å, $b = 12.786(7)$ Å, $c = 9.397(6)$ Å, $V = 1122.9$ Å^3 at $T = 297$}.[10] Its asymmetric structural unit consists of two crystallographically unique $[XeF_5]^+$ cations and a $[MnF_6]^{2-}$ anion. Each fluorine atom of the MnF_6 group is involved in secondary contacts [Xe···F(–Mn): 2.469(2)–2.583 Å] with four XeF_5 groups (Figure 1). The Mn–F bond lengths [1.796(2)–1.809(2) Å] are comparable with those found in other $[MnF_6]^{2-}$ salts, where the M^{4+} cations are located in an octahedral coordination of six fluorine atoms; for example, in Rb_2MnF_6 (1.875 Å).[11] Both crystallographically distinct $[XeF_5]^+$ cations have the typical geometry; that is, pseudo-octahedral AX_5E VSEPR arrangements of the bond pairs (X) and the lone pair (E). The Xe–F_{ax} bonds are shorter [1.817(2)/1.824(2) Å] than the remaining four Xe–F_{eq} distances [1.838(3)–1.859(3) Å]. Each XeF_5 unit forms three secondary contacts with the fluorine atoms of two MnF_6 groups (see Figure S5).

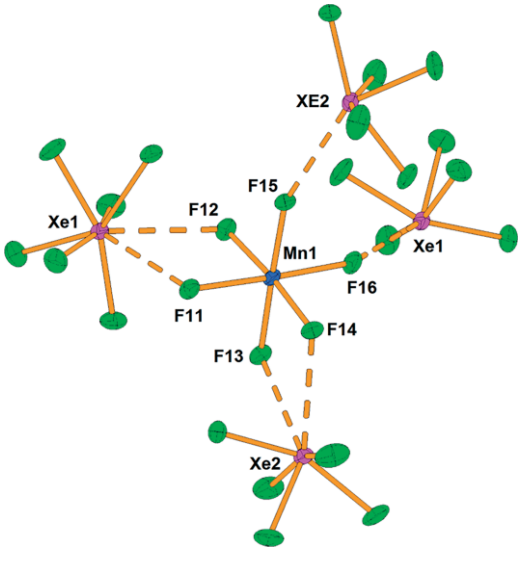

Figure 1. The secondary contacts between the $[MnF_6]^{2-}$ anion and $[XeF_5]^+$ cations in the crystal structure of $[XeF_5]_2[MnF_6]$. Thermal ellipsoids are drawn at the 50 % probability level.

Crystal Structure of XeF_5MnF_5

Single crystals of red $[XeF_5][MnF_5]$ were grown in the shape of very thin and very fragile plates. Numerous repeated attempts to get better quality structural data on single crystals of $[XeF_5][MnF_5]$ failed. Diffraction images repeatedly showed the appearance of strong "tails" around some reflections, most likely because of diffuse scattering (see Figure S6). The R-factors ($R_1 = 0.104$ and $wR_2 = 0.25$) of the best solution [orthorhombic, $Pca2_1$, $a = 17.9094(9)$ Å, $b = 9.0300(5)$ Å, $c = 8.3632(4)$ Å] were still high and the anisotropic refinement mode could be applied only for heavy atoms. Processing the data as monoclinic has improved the quality a little bit; the best result has been achieved in $P2_1/c$ space group: $a = 9.0056(4)$, $b = 17.8909(8)$, $c = 8.3748(3)$ Å, $\beta = 90.079(4)$°; all atoms refined in anisotropic mode; $R_1 = 0.094$ and $wR_2 = 0.25$ (the final refinement has been performed using a twinning matrix –1 0 0 0 –1 0 0 0 1, resulting in a 0.41 BASF parameter value). Since the unit cell and the main structural motif (infinite zigzag chains of distorted MnF_6 octahedra that share *cis* vertices) resembled that of $[XeF_5][CrF_5]$[12] (Figure S7), the attempt was made to get a better solution for the crystal structure of $[XeF_5][MnF_5]$ with the use of synchrotron X-ray powder diffraction (SXRD). The SXRD

analysis first gave the same solution [orthorhombic, $Pca2_1$, a = 17.968(1) Å, b = 9.1067(5) Å, c = 8.83874(5) Å, R_i = 0.0538] as obtained on single-crystal data. However, further detailed inspection showed that an even better solution (Figure 2) is possible (at 120 K; R_i = 0.0557) in monoclinic unit cell [at 120 K; a = 9.0265(5) Å, b = 17.8898(9) Å, c = 8.3506(5) Å, β = 90.132(5)°], where the β angle only slightly deviates from 90°.

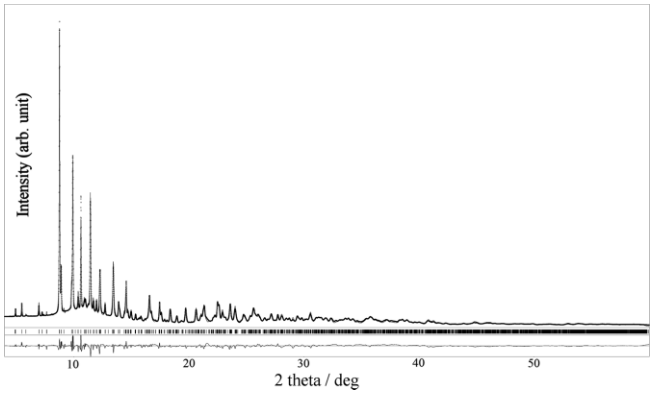

Figure 2. The experimental, calculated and difference SXRD profiles after the Rietveld refinement of $[XeF_5][MnF_5]$ (data set collected at 120 K). The obtained and calculated patterns and difference are presented by cross marks, upper solid lines and bottom solid lines, respectively. The bars mark reflection positions.

According to SXRD analysis, the crystal structure of $[XeF_5][MnF_5]$ slightly differs from $[XeF_5][CrF_5]$[12] and $[XeF_5][TiF_5]$,[5] which are isotypic. However, in all three structures, the main structural features of the anionic parts are the same; that is, infinite zigzag chains of distorted MnF_6 octahedra that share *cis* vertices (Figure 3). The crystal structure of $[XeF_5][GeF_5]$ is different because it contains infinite chains of GeF_6 octahedra sharing *trans* vertices.[13] Unfortunately, the bond lengths uncertainties in the crystal structure of $[XeF_5][MnF_5]$ are still rather high.

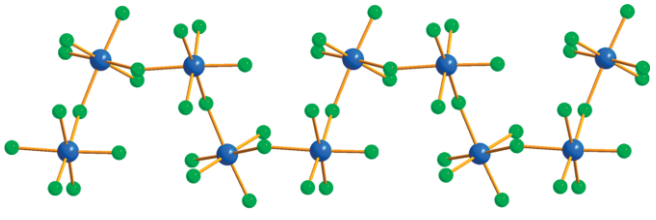

Figure 3. Part of the $([MnF_5]^-)_\infty$ infinite chain in the crystal structure of $[XeF_5][MnF_5]$.

Crystal Structure of $[XeF_5]_4[Mn_8F_{36}]$

Since crystal structures of $[XeF_5]_4[Mn_8F_{36}]$ determined at two different temperatures (150 and 296 K) are the same, it is clear that there is no phase transition in the 150–296 K range. It has been previously observed that some $[XeF_5]^+$ salts crystallize in two different modifications at low and high temperature, due to the disorder of the XeF_5 units at higher temperatures.[5,14] Crystal structure determination on single crystals of $XeF_6{\cdot}2MnF_4$ has shown that the structure is built from $[XeF_5]^+$ anions and discrete $[Mn_8F_{36}]^{4-}$ anions, resulting in a $[XeF_5]_4[Mn_8F_{36}]$ formulation. For Ti^{4+}, discrete anions with a similar formula, that is, $[Ti_8F_{36}]^{4-}$, have been determined in $K_4Ti_8F_{36}{\cdot}8HF$ and $Rb_4Ti_8F_{36}{\cdot}6HF$.[15] However, their geometry is completely different. The $[Ti_8F_{36}]^{4-}$ anion appears as a cubic species, constructed from eight TiF_6 octahedra with the eight titanium atoms situated at the vertices of a cube (Figure 4).[15] Similarly, as in $[Ti_8F_{36}]^{4-}$, each MnF_6 octahedron of $[Mn_8F_{36}]^{4-}$ shares three fluorine atoms (in *fac* position) with three neighbouring MnF_6 octahedra, resulting in a ringlike $[Mn_8F_{36}]^{4-}$ geometry (Figure 4).

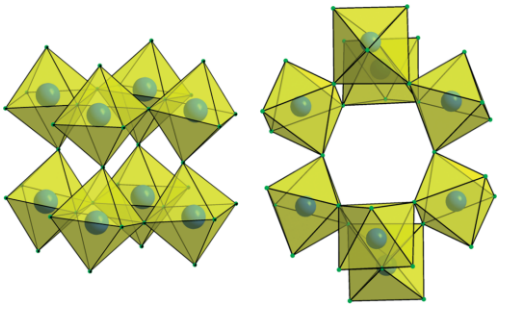

Figure 4. Comparison of geometries of the $[Ti_8F_{36}]^{4-}$[15] and $[Mn_8F_{36}]^{4-}$ anions.

Each $[Mn_8F_{36}]^{4-}$ anion forms secondary F···Xe contacts with six $[XeF_5]^+$ cations (see Figure S8). The Mn–F bond lengths can be divided into three groups. The Mn–F(···Xe) bonds, where F atoms are involved in secondary contacts with $[XeF_5]^+$ cations, are longer [1.740(2)–1.765(2) Å] than the Mn–F_t bonds [F_t = terminal fluorine atoms without further interactions; 1.710(2)–1.717(2) Å], but shorter than the Mn–F_b(–Mn) bond lengths [F_b = fluorine atoms that bridge two Mn atoms; 1.8498(19)–1.9529(19) Å; Figure 5].

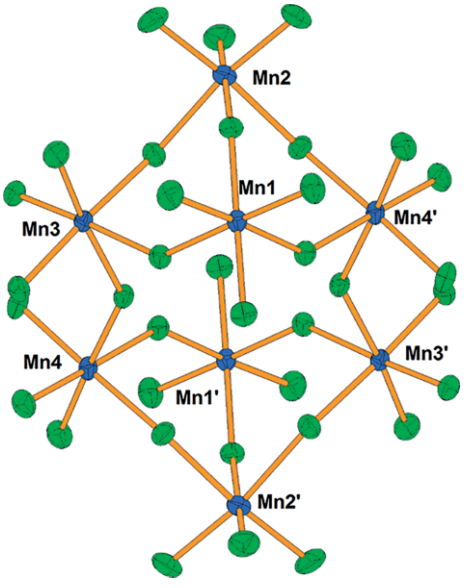

Figure 5. Discrete octameric $[Mn_8F_{36}]^{4-}$ anion in the crystal structure of $[XeF_5]_4[Mn_8F_{36}]$. Thermal ellipsoids are drawn at the 50 % probability level.

The geometries of the $[XeF_5]^+$ cations are the same as in the crystal structure of $[XeF_5]_2[MnF_6]$ [Xe1–F_{ax} = 1.796(2) Å, Xe1–F_{eq} = 1.832(2) Å, 1.849(2) Å, 1.834(2) Å and 1.812(3) Å; Xe2–F_{ax} = 1.805(2) Å, Xe2–F_{eq} = 1.833(2) Å, 1.838(2) Å, 1.840(2) Å

and 1.835(2) Å]. The Xe1 forms three secondary contacts, Xe···F(–Mn), with two with F atoms of two $[Mn_8F_{36}]^{4-}$ anions; meanwhile, the Xe2 forms four secondary contacts, Xe···F(–Mn), with F atoms of the same $[Mn_8F_{36}]^{4-}$ anion (see Figure S8). The crystal structure of $O_2Mn_2F_9$[16] represents a rare case of ternary manganese(IV) fluoride compound, where the anionic part is not just a simple octahedral $[MnF_6]^{2-}$ anion. The $[Mn_2F_9]^-$ anion is an infinite dimeric zigzag chain composed of MnF_6 octahedra sharing vertices. It can be imagined as being constructed from two single chains of $([MnF_5]^-)_\infty$ (as observed in $[XeF_5][MF_5]$) that additionally share some vertices to form a double $([Mn_2F_9]^-)_\infty$ chain (see Figure S9). The Mn–F_t bond lengths (1.73–1.76 Å) and Mn–F_b(–Mn) (1.88–1.90 Å) bond lengths are close to those found in $[XeF_5]_4[Mn_8F_{36}]$.

Magnetic Properties of $[XeF_5][MnF_5]$

For $[XeF_5][MnF_5]$, it was previously reported that it is paramagnetic and that it obeys the Curie–Weiss law in the 4–290 K temperature range (μ_{eff} = 3.89 μ_B and θ = –8 K).[2] Crystal structure determination showed that the crystal structure of $[XeF_5][MnF_5]$ consists of $([MnF_5]^-)_\infty$ infinite chains, where neighbouring Mn atoms are connected via F bridges. Since superexchange interactions between Mn atoms via Mn–F–Mn bridges are possible, we decided to do more detailed analysis of the magnetic properties of $[XeF_5][MnF_5]$.

Results of magnetic susceptibility measurements in magnetic fields of 100 Oe, 1000 Oe and 10 kOe are shown in Figure S11. The susceptibility is practically independent of the applied magnetic field. Above 60 K, it monotonically decreases with increasing temperature, and as we will show later, follows a Curie–Weiss law. At 50 K, the zero-field-cooled (zfc) susceptibility exhibits a bump, and below 50 K, it significantly differs from the field-cooled susceptibility measured on cooling the sample in a magnetic field (fc on cooling). At first glance, the behaviour below 50 K can be attributed to the interesting magnetic properties. However, as the zfc susceptibility is larger than the fc susceptibility on cooling, which is opposite to that usually measured in magnetically ordered systems, we studied the temperature and time dependence of the susceptibility in more detail.

When the temperature rate was reduced from 2 K min^{-1} (with a bump at 50 K) to 0.4 K min^{-1}, the bump shifted to 15 K (see the blue curve in Figure S11). With this sample rate, the susceptibility was also measured on heating the sample after it was cooled in a magnetic field (fc on heating). The difference between the zfc and fc curves, in this case, practically vanishes (see the inset in Figure S11).

As the position of the bump depends on the heating rate and the bump is completely absent for the measurements during the cooling of the sample (fc on cooling), we tried to find out whether the peculiar magnetic behaviour is an intrinsic magnetic property or whether it is only a thermal effect. By "thermal effect", we mean the possibility that the temperature of the sample does not sufficiently quickly follow the sample space temperature that is measured and reported by the MPMS-XL-5 magnetometer. In this case, on heating, the temperature of the sample would be lower than the reported temperature, while on cooling, the sample temperature would be larger than the reported temperature, and, for example, for the paramagnetic signal, the measured magnetization would be smaller than it should be at a given temperature. To check the thermal contact between the sample holder (evacuated and sealed quartz tube) and the sample, we transferred the sample into a small capsule made of Teflon™. The measured temperature-dependent susceptibility was the same as that already described in Figure S11, with the sample in a quartz tube. In addition, similar measurements were performed with a paramagnetic K_2MnF_6 sample in the same quartz tube as used for $[XeF_5][MnF_5]$. The result – paramagnetic behaviour with no difference between zfc and fc susceptibility – for K_2MnF_6 is shown in Figure S12, with no indication of any thermal contact problems. We can conclude the thermal contact between the sample and the sample holder was good enough and cannot be responsible for the zfc and fc susceptibility differences of $[XeF_5][MnF_5]$ at low temperatures.

Finally, the magnetization of $[XeF_5][MnF_5]$ as a function of temperature was measured extremely slowly. In Figure 6a, we show time-dependent magnetization after a zero-field protocol between 2 K and 8 K in a constant magnetic field of 1000 Oe. The time t = 0 was set at the moment the sample had reached the lowest temperature of 2 K and the magnetic field had been turned on. We can observe a slow time dependence of the magnetization that does not saturate, even after 60 min. At t = 60 min, the temperature was increased to 3 K, and again, the

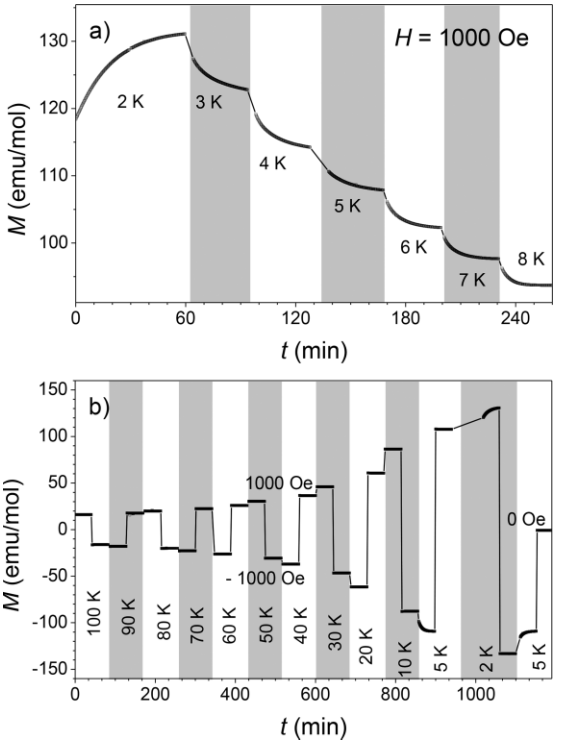

Figure 6. (a) Time-dependent magnetization $M(t)$ after the zfc protocol in a constant magnetic field of 1000 Oe at temperatures of 2 K, 3 K,···8 K. (b) $M(t)$ at 100 K, 90 K···2 K and 5 K after changing the magnetic field from 1000 Oe to –1000 Oe or vice versa at a constant temperature.

magnetization showed a slow time decay. The change of the magnetization during relaxation, over 30 min at a constant sample-chamber temperature and constant magnetic field, amounts to approximately 10 % of the terminal magnetization. Such an effect can clearly be responsible for the peculiar magnetic behaviour observed in Figure S11.

There are at least two possible explanations for the observed time decay of magnetization. Very slow time decay of "thermoremanent magnetization" can be observed in magnetically frustrated systems, like spin glasses,[17] or geometrically frustrated systems.[18] The alternative explanation of the effect observed in Figure 6a can be slow thermal stabilization of the sample: the magnetization decays because the sample needs a relatively long time to reach the new temperature. To distinguish between these two possibilities, we performed the following experiment. The sample was cooled to 100 K in H = 1000 Oe (Figure 6b). After recording the magnetization for 30 min, the magnetic field was changed to –1000 Oe, still at 100 K. The magnetization changed the sign; no slow time decay was observed. In the next step, the temperature was reduced to 90 K in H = –1000 Oe. After 30 min of measurements, the magnetic field was changed to a positive value of 1000 Oe and magnetization was recorded for another 30 min before the temperature was decreased again. Below 10 K, we observed a slow relaxation of magnetization generated by the temperature change from 10 to 5 K, 5 K to 2 K and finally, from 2 K to 5 K. The field changes at any temperature (even at 2 K) are not accompanied by a slow relaxation. We can conclude that the slow time decays of magnetization are provoked by a slow thermal stabilization of the sample and are not a magnetic property. As we previously demonstrated good thermal contact between the sample and sample holder, we tentatively contribute slow thermal stabilization of the sample to a low thermal conductivity of the $[XeF_5][MnF_5]$.

In Figure 7a, the susceptibility measured in a magnetic field of 1000 Oe is shown after the zfc and fc protocols. At each temperature, the sample was left 30 min for thermal stabilization. Now, there is no difference between the zfc and fc curves. The full green curve is a Curie–Weiss fit $\chi = C/(T - \theta)$ for $T >$ 100 K, with a Curie constant of C = 1.87 emu K mol^{-1} and a Curie–Weiss temperature of θ = –9.3 K. The calculated effective magnetic moment $\mu_{eff} = 8C$ = 3.87 μ_B exactly corresponds to the theoretical value for a Mn^{IV} ion with quantum spin numbers $J = S$ = 3/2, L = 0.[19] Isothermal magnetization at 2 K and 5 K is shown in Figure 7b. The curves are almost identical and are practically linear. Even at the largest magnetic field of 50 kOe, the magnetization is far from the theoretical saturation value of $gS\mu_B$ = 3 μ_B.

The linear $M(H)$, even at the lowest temperature, the negative Curie–Weiss temperature θ, and decrease of the effective magnetic moment, μ_{eff}, below 100 K (inset in Figure 7a) indicate a weak antiferromagnetic interaction between the Mn^{IV} ions.

The nearest-neighbour Mn^{IV} ions are bridged by a single bridging fluorine atom and make a quasi-one-dimensional structure of 3/2 spins. Unfortunately, there is no analytical function describing a temperature-dependent susceptibility $\chi(T)$ of a chain of S = 3/2 spins, as can be found[20] for spins S = 1/2,

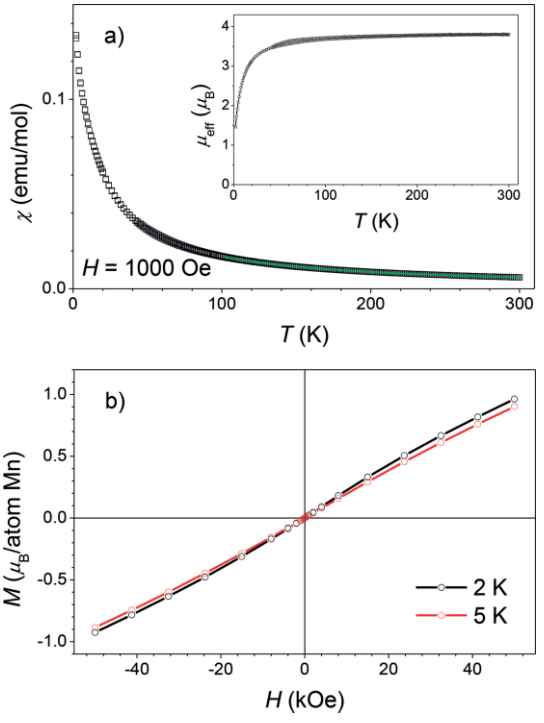

Figure 7. (a) The magnetic susceptibility vs. temperature of $[XeF_5][MnF_5]$, measured in magnetic field of 1000 Oe, after the zfc and fc protocols. At each temperature, the sample was left 30 min for thermal stabilization. The full green curve represents a Curie–Weiss fit for $T >$ 100 K with C = 1.87 emu K mol^{-1} and θ = –9.3 K. (b) Isothermal magnetization at 2 K and 5 K.

S = 1 and S = 5/2 or above, where for the latter, the spin may be treated as a classical vector. Thus, we will use a crude approximation and apply the result of mean field theory[19] for the chain with z = 2 nearest neighbours and estimate the interaction parameter, J:

$$\frac{J}{k_B} = \frac{3\vartheta}{2zS(S+1)} \approx -1.3 \text{ cm}^{-1}$$

Conclusion

Crystal structure determination of $2XeF_6 \cdot MnF_4$ confirmed a previous assumption that it can be described as $[XeF_5]_2[MnF_6]$.[3] In the case of $[XeF_5][MnF_5]$ ($XeF_6 \cdot MnF_4$), it has been found that the main structural feature of the anionic part is similar to that in $[XeF_5][MF_5]$ (M = Cr,[12] Ti[5]), although the compounds are not isotypic. In the case of magnetic investigation of $[XeF_5][MnF_5]$, we wanted to emphasize the importance of carefully implemented experiments that help us understand the apparent complicated temperature-dependent magnetism as a purely thermal effect.

The most interesting case had represented the answer to the question about the crystal structure of $XeF_6 \cdot 2MnF_4$, where XeF_6 acts as single fluoride ion donor providing one F^- anion per two MnF_4 molecules. Possible options for the geometry of the anionic Mn part were infinite discrete dimeric $[Mn_2F_9]^-$ (as theoretically predicted,[21] but experimentally never shown $[Ti_2F_9]^-$ [22]), $([Mn_2F_9]^-)_\infty$ double chains {different geometries as

$([Ti_2F_9]^-)_\infty$ in $CsTi_2F_9$[22] or $([Mn_2F_9]^-)_\infty$ in O_2MnF_9[16] shown in Figure S10}, discrete prismatic $[Mn_6F_{27}]^{3-}$ (as $[Ti_6F_{27}]^{3-}$ in $[ImH]_2[H_3O][Ti_6F_{27}]$[23]), discrete tetrameric $[Mn_4F_{18}]^{2-}$ (as $[Ti_4F_{18}]^{2-}$ in $[Me_4N]_2[Ti_4F_{18}]$[22]), discrete octameric $[Mn_8F_{36}]^{4-}$ cubes (as $[Ti_8F_{36}]^{4-}$ in $K_4Ti_8F_{36}$·8HF and $Rb_4Ti_8F_{36}$·6HF[15]), discrete double-star-shaped $[Mn_{10}F_{45}]^{5-}$ (as $[Ti_{10}F_{45}]^{5-}$ in $[XeF_5]_4[Ti_{10}F_{45}]$[5]) or a three-dimensional $([Mn_6F_{27}]^{3-})_\infty$ framework {as $([Ti_6F_{27}]^{3-})_\infty$ in $(H_3O)_3[Ti_6F_{27}]$[23]}. In all listed cases, the AF/MF_4 ratio corresponds to 1:2, where AF represents a single fluoride ion donor and MF_4 contains metal in the oxidation state M^{4+}. Crystal structure determination of XeF_6·$2MnF_4$ has revealed that the structure is built from $[XeF_5]^+$ cations and discrete $[Mn_8F_{36}]^{4-}$ anions. This is contrary to XeF_6·$2TiF_4$, that is, $[XeF_5]_5[Ti_{10}F_{45}]$, which consists of $[XeF_5]^+$ cations and discrete $[Ti_{10}F_{45}]^{5-}$ anions.[5] The discrete oligomeric $[Ti_8F_{36}]^{4-}$ anions have also been determined in $K_4Ti_8F_{36}$·8HF and $Rb_4Ti_8F_{36}$·6HF. However, the geometry of the $[Ti_8F_{36}]^{4-}$ anion is completely different from $[Mn_8F_{36}]^{4-}$; that is, the $[Ti_8F_{36}]^{4-}$ anion appears as a cubic species, while in $[Mn_8F_{36}]^{4-}$, the MnF_6 octahedra form a ring.

Experimental Section

CAUTION: Anhydrous HF and some fluorides are highly toxic and must be handled in a well-ventilated hood, and protective clothing must be worn at all times! XeF_6 and all of its products are susceptible to moisture and react with water to form XeO_3, a shock-sensitive compound that detonates easily.

Materials and Methods

Reagents: Anhydrous HF (Linde AG, Pullach, Germany, 99.995 %) was treated with K_2NiF_6 (Advance Research Chemicals, Inc.) for several hours prior to use. The MnF_2 (Alfa Aesar, 99 %) was used as supplied. The MnF_3 was synthesized as described previously.[24] Xenon difluoride was prepared by the photochemical reaction between Xe and F_2 at ambient temperature.[25]

Synthetic Apparatus: All the manipulations were carried out under anhydrous conditions. The volatile compounds, such as aHF and F_2, were handled in a vacuum line constructed from nickel–Teflon™ and the nonvolatile materials were handled in a dry box (M. Braun) in an argon atmosphere (< 0.5 ppm H_2O). Single crystals were grown in T-shaped crystallization vessels composed of two FEP (tetrafluoroethylene-hexafluoropropylene block copolymer; Polytetra GmbH, Germany) tubes (one 16 mm i.d., 19 mm o.d. and the other 4 mm i.d., 6 mm o.d.) equipped with PTFE valves. Before use, the abovementioned crystallization vessels were passivated with elemental fluorine (Solvay).

Synthesis and Crystal Growth in XeF_6/MnF_4 System

Various amounts of XeF_2 and MnF_3 were loaded into reaction vessel inside a drybox (Table S1). Anhydrous HF (5–10 mL) was condensed onto the solid at 77 K and the reaction mixture was brought to ambient temperature. Fluorine was slowly added at ambient temperature to a pressure of 6 bar in the reaction vessel. A medium pressure mercury lamp (Hg arc lamp, 450 W, Ace Glass, USA) was used as the UV source. The reaction mixture was left stirring for 10–29 days at ambient temperature. All volatile substances were slowly pumped off at ambient temperature, leaving orange or red solids (Table S1). After characterization, powdered products were transferred to the crystallization vessels, where aHF (6–10 mL) was condensed onto the starting material at 77 K. The crystallization mixture was warmed to ambient temperature and the resulting clear solution was decanted into the 6 mm o.d. side arm. Evaporation of the solvent from this solution was carried out by maintaining a temperature gradient of ca. 10–20 °C between both tubes for several weeks. Slow distillation of aHF from the 6 mm o.d. tube into the 19 mm o.d. tube resulted in crystal growth inside the 6 mm o.d. tube.

Several solutions of dissolved products, prepared from $n XeF_2/MnF_3$/UV-irradiated F_2/aHF mixtures in crystallization vessels, were left to crystallize without prior isolation and characterization.

Selected single crystals were transferred to 0.3 mm quartz capillaries inside the dry box and their Raman spectra were recorded at several random positions. In some cases, the Raman spectra were also measured on powdered crystals. All Raman spectra are shown and discussed in the Supporting Information.

X-ray Single-Crystal Structure and Synchrotron Powder Crystal Structure Determinations

Crystals were immersed in perfluorodecalin (Fluorochem, Cat. Code: 003283, melting point 263 K) inside a dry box, selected under a microscope and mounted on the goniometer head of the diffractometer in a cold nitrogen stream. Crystals sealed in quartz-glass capillaries were used for the structure determination at room temperature.

Single-crystal data for $[XeF_5]_2[MnF_6]$ and $[XeF_5]_4[Mn_8F_{36}]$ were collected with a Gemini A diffractometer equipped with an Atlas CCD detector, using graphite monochromated Mo-K_α radiation. The data were treated with the CrysAlisPro software suite program package.[26] Analytical absorption corrections were applied to all the data sets. The structures were solved with the charge-flipping method using the Superflip program[27] (Olex crystallographic software).[28] The electron density map, obtained with the Superflip software, was analyzed with the EDMA program,[29] which gave initial models of the structures. Some structures were solved with the SHELXS program.[30] Structure refinement was performed with the SHELXL-2014[31] software, implemented in the program package WinGX.[32] The figures were prepared using the DIAMOND 4.3 software.[33] In a similar manner, many crystals of $[XeF_5][MnF_5]$ were measured, resulting only in an initial structure model. Powdered samples were studied at the Materials Science Beamline at PSI (Villigen, Switzerland), with the Mythen II detector and λ = 0.774956 Å. Data were measured on powder samples ground under inert conditions at three different temperatures (120 K, 150 K and 200 K). The samples were placed into thin-walled glass capillaries. The final refinement of the last structure was performed against powder diffraction data, by the Rietveld method, using WinCSD software.[9]

Further details of the crystal structure investigation(s) may be obtained from Fachinformationszentrum Karlsruhe, 76344 Eggenstein-Leopoldshafen, Germany (fax: +49-7247-808-259; e-mail: crysdata@fiz-karlsruhe.de, http://www.fiz-karlsruhe.de/request_for_deposited_data.html), on quoting the deposition numbers CSD-432503 (for $[XeF_5]_2[MnF_6]$), -432505 (for $[XeF_5][MnF_5]$, 120 K) and -432504 (for $[XeF_5]_4[Mn_8F_{36}]$, 150 K).

Raman Spectroscopy: Raman spectra, with a resolution of 0.5 cm^{-1}, were recorded at room temperature with a HORIBA JOBIN YVON LabRam-HR spectrometer equipped with an Olympus BXFM-ILHS microscope. Samples were excited with the 632.8 nm emission line of a He–Ne laser with the power 20 mW, which equates to a power of 17 mW focused onto a 1 µm spot through a 50× microscope objective on the top surface of the sample. The power of the beam was varied from 17 mW to 1.7 mW. The laser power above 1.7 mW led to decomposition of $[XeF_5]_2[MnF_6]$ and $[XeF_5][MnF_5]$

(see Supporting Information). The Raman spectra of $[XeF_5]_2[MnF_6]$ and $[XeF_5][MnF_5]$ were also acquired on the randomly orientated single crystals. All crystals were first checked with a diffractometer.

Magnetic Measurements: Temperature-dependent magnetic susceptibility between 2 K and 300 K and isothermal magnetization between –50 kOe and 50 kOe were measured with a Quantum Design MPMS-XL-5 SQUID magnetometer. All presented data were corrected for a temperature-independent diamagnetic contribution of inner-shell electrons, as obtained from Pascal's tables.[20]

Supporting Information (see footnote on the first page of this article): Raman spectra of $[XeF_5]_2[MnF_6]$ (Figure S1) and $[XeF_5][MnF_5]$ (Figure S2) prepared by photochemical reaction; Raman spectrum of $[XeF_5]_2[MnF_6]$, prepared by reaction between XeF_6, MnF_2 and KrF_2 in aHF (Figure S3); Raman spectrum of $[XeF_5]_2[MnF_6]$, prepared by reaction between XeF_6 and MnO_3F in aHF (Figure S4) and a short notification of results of reactions between MnO_2, MnO_3F and different fluorinating agents (F_2, UV-irradiated F_2, XeF_6, KrF_2) in aHF; secondary Xe···F interactions between $[XeF_5]^+$ cations and $[MnF_6]^{2-}$ anions in the crystal structure of $[XeF_5]_2[MnF_6]$ (Figure S5); two X-ray diffraction images measured on a single crystal of $[XeF_5][MnF_5]$ (Figure S6); part of the $([CrF_5]^-)_\infty$ chain in the crystal structure of $[XeF_5][CrF_5]$ (Figure S7); secondary Xe···F interactions between $[Mn_8F_{36}]^{4-}$ anion and $[XeF_5]^+$ cations in the crystal structure of $[XeF_5]_4[Mn_8F_{36}]$ (Figures S8 and S9); dimeric $([Mn_2F_9]^-)_\infty$ chain in $O_2Mn_2F_9$ (Figure S10); preliminary results of magnetic susceptibility measurements of $[XeF_5][MnF_5]$ (Figure S11); results of magnetic susceptibility measurements of K_2MnF_6 (Figure S12); and experimental conditions for photochemical syntheses and observed xenon(VI) hexafluoridomanganates(IV) (Table S1).

Acknowledgments

Z. M., E. G. and Z. J. acknowledge the financial support from the Slovenian Research Agency (research core funding no. P1-0045 and no. P2-0348). This work was supported by the Fonds de la Recherche Scientifique (FNRS) (PDR T.0169.13.) We thank the Paul Scherrer Institute (PSI) for the beam time allocation at the MS beamline and Dr. Voraksmy Ban for assistance.

Keywords: Manganese · Fluorides · Xenon hexafluoride · Structure elucidation · Magnetic properties

[1] G. J. Aubert, G. H. Cady, *Inorg. Chem.* **1970**, *9*, 2600–2602.
[2] M. Bohinc, J. Grannec, J. Slivnik, B. Žemva, *J. Inorg. Nucl. Chem.* **1976**, *38*, 75–76.
[3] A. Jesih, B. Žemva, *Vestn. Slov. Kem. Drus.* **1991**, *38*, 161–168 (in English).
[4] B. Žemva, J. Slivnik, M. Bohinc, *J. Inorg. Nucl. Chem.* **1976**, *38*, 73–74.
[5] Z. Mazej, E. Goreshnik, *New J. Chem.* **2016**, *40*, 7320–7325.
[6] Z. Mazej, E. Goreshnik, *Eur. J. Inorg. Chem.* **2009**, 4503–4506.
[7] Z. Mazej, "Photochemical Syntheses of Fluorides in Liquid Anhydrous Hydrogen Fluoride" in *Progress in Fluorine Science Vol. 3: Modern Synthesis Processes and Reactivity of Fluorinated Compounds* (Eds.: H. Groult, F. Leroux, A. Tressaud), Academic Press, London, **2017**.
[8] Z. Mazej, *J. Fluorine Chem.* **2002**, *114*, 75–80.
[9] L. Akselrud, Y. Grin, *J. Appl. Crystallogr.* **2014**, *47*, 803–805.
[10] K. Leary, D. H. Templeton, A. Zalkin, N. Bartlett, *Inorg. Chem.* **1973**, *12*, 1726–1730.
[11] P. Bukovec, R. Hoppe, *J. Fluorine Chem.* **1988**, *38*, 107–114.
[12] K. Lutar, H. Borrmann, B. Žemva, *Inorg. Chem.* **1998**, *37*, 3002–3006.
[13] T. E. Mallouk, B. Desbat, N. Bartlett, *Inorg. Chem.* **1984**, *23*, 3160–3166.
[14] Z. Mazej, E. Goreshnik, *Eur. J. Inorg. Chem.* **2016**, 3356–3364.
[15] I. M. Shlyapnikov, E. A. Goreshnik, Z. Mazej, *Chem. Commun.* **2013**, *49*, 2703–2705.
[16] B. G. Müller, *J. Fluorine Chem.* **1981**, *17*, 409–421.
[17] J. A. Mydosh, *Spin Glasses: An Experimental Introduction*, Taylor and Francis, London, **1993**.
[18] P. Koželj, S. Jazbec, S. Vrtnik, A. Jelen, J. Dolinšek, M. Jagodič, Z. Jagličić, P. Boulet, M. C. de Weerd, J. Ledieu, J. M. Dubois, V. Fournee, *Phys. Rev. B* **2013**, *88*, 214202.
[19] N. W. Ashcroft, N. D. Mermin, *Solid State Physics*, Saunders College Publishing, Philadelphia, **1976**.
[20] O. Kahn, *Molecular Magnetism*, VCH Publishing, New York, **1993**.
[21] A. Decken, H. D. B. Jenkins, C. Knapp, G. B. Nikiforov, J. Passmore, J. M. Rautiainen, *Angew. Chem. Int. Ed.* **2005**, *44*, 7958–7961; *Angew. Chem.* **2005**, *117*, 8172.
[22] Z. Mazej, E. Goreshnik, *Inorg. Chem.* **2009**, *48*, 6918–6923.
[23] Z. Mazej, I. M. Shlyapnikov, E. Goreshnik in *The First South African Fluorine Symposium: Book of Abstracts*, South African Department of Science and Technology, Cape Town, February **2016**, p. 47.
[24] Z. Mazej, K. Lutar, B. Žemva, *Acta Chim. Slov.* **1999**, *46*, 229–238.
[25] A. Šmalc, K. Lutar in *Inorganic Syntheses* (Ed.: R. N. Grimes), Wiley, New York, **1992**, vol. 29, p. 1.
[26] *CrysAlisPro*, Agilent Technologies, Version 1.171.37.31 (release 14–01–**2014** CrysAlis171.NET).
[27] L. Palatinus, G. Chapuis, *J. Appl. Crystallogr.* **2007**, *40*, 786–790.
[28] O. V. Dolomanov, L. J. Bourhis, R. J. Gildea, J. A. K. Howard, H. Puschmann, *J. Appl. Crystallogr.* **2009**, *42*, 339–341.
[29] L. Palatinus, S. Jagannatha Prathapa, S. van Smaalen, *J. Appl. Crystallogr.* **2012**, *45*, 575–580.
[30] G. M. Sheldrick, *Acta Crystallogr., Sect. A* **2008**, *64*, 112–122.
[31] G. M. Sheldrick, *Acta Crystallogr., Sect. C* **2015**, *71*, 3–8.
[32] L. J. Farrugia, *J. Appl. Crystallogr.* **2012**, *45*, 849–854.
[33] H. Putz, K. Brandenburg, *Diamond: Crystal and Molecular Structure Visualization Crystal Impact*, Dr. H. Putz & Dr. K. Brandenburg GbR, Kreuzherrenstr. 102, 53227 Bonn, Germany http://www.crystalimpact.com/diamond.

Received: January 17, 2017